Materials and Design 186 (2020) 108337

Contents lists available at ScienceDirect

Materials and Design

journal homepage: www.elsevier.com/locate/matdes

Low gas consumption fabrication of ^{3}He solid targets for nuclear reactions

Asunción Fernández [a,*], Dirk Hufschmidt [a], Julien L. Colaux [b,c], Jose Javier Valiente-Dobón [d], Vanda Godinho [a], Maria C. Jiménez de Haro [a], David Feria [a], Andrés Gadea [e], Stéphane Lucas [c]

[a] Instituto de Ciencia de Materiales de Sevilla, CSIC-Univ. Seville, Avda. Américo Vespucio 49, 41092 Seville, Spain
[b] Synthesis, Irradiation & Analysis of Materials (SIAM) Platform, University of Namur, 61 Rue de Bruxelles, 5000 Namur, Belgium
[c] Laboratoire d'Analyse par Réactions Nucléaires (LARN), Namur Institute of Structured Matter (NISM), University of Namur, 61 Rue de Bruxelles, 5000 Namur, Belgium
[d] INFN, Laboratori Nazionali di Legnaro, Legnaro, Italy
[e] Instituto de Física Corpuscular, CSIC-Univ. Valencia, E-46980 Paterna, Spain

HIGHLIGHTS

- Fabrication of ^{3}He nanocomposite films as solid targets for nuclear reactions
- More than 99.5% reduction in ^{3}He gas consumption by quasistatic sputtering deposition
- The ^{3}He content was over 1×10^{18} at/cm^2 for foil thicknesses between 1.5 and 3 μm.
- Targets show adequate stability for reactions performed in inverse kinematic.

GRAPHICAL ABSTRACT

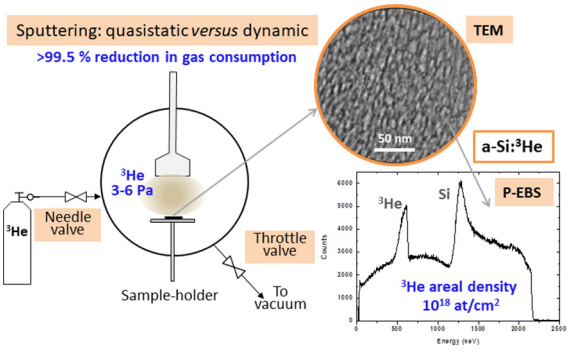

ARTICLE INFO

Article history:
Received 7 August 2019
Received in revised form 5 November 2019
Accepted 6 November 2019
Available online 07 November 2019

Keywords:
He-3 solid targets
Quasistatic magnetron sputtering
Low gas consumption
Nuclear reactions
Inverse kinematics
Target stability

ABSTRACT

Nanoporous solids that stabilize trapped gas nanobubbles open new possibilities to fabricate solid targets for nuclear reactions. A methodology is described based on the magnetron sputtering (MS) technique operated under quasistatic flux conditions to produce such nanocomposites films with ^{3}He contents of up to 16 at.% in an amorphous-silicon matrix. In addition to the characteristic low pressure (3–6 Pa) needed for the gas discharge, the method ensures almost complete reduction of the process gas flow during film fabrication. The method could produce similar materials to those obtained under classical dynamic flux conditions for MS. The drastic reduction (>99.5%) of the gas consumption is fundamental for the fabrication of targets with scarce and expensive gases. Si:^{3}He and W:^{3}He targets are presented together with their microstructural (scanning and transmission electron microscopy, SEM and TEM respectively) and compositional (Ion Beam Analysis, IBA) characterization. The ^{3}He content achieved was over 1×10^{18} at/cm^2 for film thicknesses between 1.5 and 3 μm for both Si and W matrices. First experiments to probe the stability of the targets for nuclear reaction studies in inverse kinematics configurations are presented.

* Corresponding author.
E-mail address: asuncion@icmse.csic.es (A. Fernández).

https://doi.org/10.1016/j.matdes.2019.108337

1. Introduction

An increasing interest in developing light gas targets for nuclear science and high energy density research has been developed in recent years [1–5]. In nuclear physics the advent of radioactive beam facilities will allow to further probe stability and to uncover in detail the nature of the nucleus-nucleus interaction. In this endeavour, transfer reactions have been demonstrated as optimal to identify the behaviour of nuclear forces. In contrast with studies where stable beams are used, when one uses radioactive ion beams, the reactions are performed in inverse kinematics, i.e., the heavy beam on a light target [1,2]. Due to the gaseous nature of most of the light target ions of interest, gas targets (i.e., He, Ne and H isotopes) for nuclear structure and reaction studies have been developed [3,6,7]. Gas targets or gas cells can also be used for the production of radioactive isotopes [8] or for the fabrication of particle detectors (i.e., neutrons) [9].

Depending on the application gas cells [1], foils with implanted gases [10,11], windowless gas targets [12,13], cryogenic targets [14], or active targets [15,16] have been used. The requirements of the targets depend on the specific application [1,3]. Limitations may be considered for different types of targets with respect to different aspects, such as compatibility with the detection setup in each particular experiment; low stability; low gas (mass/cm^2) and high impurity contents; background reactions and straggling by cells windows [1,3]; or large gas consumption, for example, in windowless gas jet devices [12,13].

In this context, we have previously proposed a novel type of "solid He targets" [17] composed of gas nanobubbles trapped within a nanoporous solid matrix that are able to stabilize the gas at ultrahigh density and pressure in ambient conditions [18–20]. These targets have been fabricated by magnetron sputtering in the form of self-supported foils, or supported on adequate substrates, and allow areal atomic densities of 4×10^{18} at/cm^2 to be achieved for helium in amorphous silicon [17]. These nanocomposite films can overcome limitations of cryogenic or gas cell based systems, which are bulky and difficult to handle, thus facilitating usage, reducing energy straggling effects and simplifying geometry for calculations. Also the thin film nature and the stability of the trapped gas targets make them unique for specific experiments, such as those devoted to lifetime measurements [21]. There are papers in the literature that also refer to the incorporation of the process gas in coatings grown by MS. These works are however mainly oriented to understand the mechanism of He trapping and materials degradation in nuclear technology [22].

The present paper demonstrates how the proposed methodology could be suited for cases of scarce, radioactive or expensive gases by drastically reducing the gas consumption during fabrication. This methodology is a research breakthrough, especially for targets enriched in expensive and strategic gases such as the ^{3}He isotope. A previous work [23] showed the formation of TiH_xHe films by MS using hydrogen-helium-argon mixtures as process gas. The work aimed to investigate the damage (helium embrittlement) in hydride materials. ^{4}He and hydrogen have been used instead of ^{3}He and tritium which are the ones of final interest for the nuclear sector. The methodology presented here is thought to make these target materials accessible by radically reducing the gas consumption during fabrication. In addition to fabrication and characterization the paper also shows first evaluation and testing of the ^{3}He-rich solid nanocomposite films for nuclear reactions in inverse kinematic configuration.

Also different topics have been recently referred for laser driven high energy-density plasma investigations: Laser driven inertial confinement fusion [4,24], laser driven high energy ion beams generation [25], or the irradiation of deuterated nanostructures with ultrafast lasers to efficiently create ultra-high energy density plasmas and drive D-D fusion reactions [5]. The here presented methodology to fabricate easy to handle "solid-gas" nanocomposite films as ^{4}He and ^{3}He targets could be potentially relevant also in these fields.

The strategic value of the materials and methodology presented in this paper has been proved at the laboratory scale for research purposes. The low consumption strategy has been crucial for running multiple experiments in the laboratory for on demand design with a low cost. Future relevance is however envisaged when considering the strategic value, and actual concerns about resources, of the ^{3}He isotope [26].

2. Experimental section

The ^{3}He-rich solid targets were prepared within a conventional magnetron sputtering deposition chamber modified to operate in an innovative static or quasistatic [27] procedure. Due to pressure fluctuations during film deposition, fully static conditions are not possible. Experimental modifications were necessary to perform very small adjustments to the working pressure (i.e., quasistatic conditions), as described in detail in the "Results and discussion" section. The chamber is equipped with a 2-inch magnetron head with a target to sample-holder distance of 10 cm. Si (99.999% purity, Neyco) and W (99.95% purity, Neyco) cathodes were used for the fabrication of Si:He, Si:^{3}He, W:He and W:^{3}He samples. Helium (He) as process gas refers to the natural isotope distribution (mainly ^{4}He) as supplied by Air Liquide (99.999%). ^{3}He refers to the pure isotope as received from Chemgas (≥99.9%). Table 1 summarizes the nomenclature of the investigated samples along with the experimental parameters used for their synthesis. In the case of natural He the use of dynamic or static mode is indicated in the sample label. The thin films were synthesized on a variety of substrates demonstrating the versatility of the deposition technique. Silicon substrates were typically 525 μm thick (100) wafers, while gold substrates were foils of 10 mg/cm^2.

The thickness and morphology of the films were examined by scanning electron microscopy (SEM) by employing a HITACHI S-4800 SEM-FEG microscope. The samples deposited on silicon substrates were cleaved and observed as such in cross-sectional views at 1–2 kV.

The nanostructure of the nanocomposite films was investigated at the Laboratory of Nanoscopies and Spectroscopies (LANE-ICMS, Sevilla, Spain) by Transmission Electron Microscopy (TEM) using a Jeol 2100Plus and a Tecnai G2 F30 TEM operated at 200 and 300 kV, respectively. The cross sectional TEM samples were prepared by mechanical polishing and dimple grinding of the coatings deposited on silicon, followed by Ar^+ ion milling to electron transparency. The pore distribution was evaluated from TEM micrographs by binarizing them and using the "Analyze Particle" function of ImageJ software [28].

The elemental depth profiles of the coatings were determined by IBA (ion beam analysis) techniques at the SIAM (synthesis, irradiation and analysis of materials) platform of the University of Namur (Belgium) using a 2M-Tandetron Linear Accelerator from HVEE. A general discussion about thin films depth profiling by IBA can be found in Ref. 29. Samples grown on silicon substrates were measured as received using proton- or alpha-beams in the following conditions:

i) With the alpha-beam, the samples were first analyzed at 2.4 MeV in tilted incidence to determine the H content by ERD (elastic recoil detection). Then EBS (elastic backscattering spectrometry) spectra were collected from the same location at various incident energies, namely, at 3.05 MeV to determine the oxygen content [30], at 3.75 MeV to determine the nitrogen content [31], and at 4.3 MeV to determine the carbon content [32].
ii) Proton-beam at 2.5 MeV for sensitivity to helium by proton-EBS (p-EBS). It should be noted that the ^{3}He signal observed by p-EBS was well resolved from the ^{4}He signal because of the variation of the kinematic factor. For the data reduction, the ^{3}He(p,p)^{3}He cross-section measured by Langley [33] and that of ^{4}He(p,p)^{4}He provided by SigmaCalc [34] were used.

The particle (PIPS) detectors were set at 165, 135 and 30 degrees relative to the incident beam direction, while the PIXE (particle-induced X-ray emission) detector was mounted at 135 degrees opposite to the PIPS

Table 1
Nomenclature and deposition parameters for the investigated samples.

Sample	Deposition procedure	Substrate[a]	He or ^{3}He pressure (Pa)	RF power (W)	Deposition time (h)	Thickness[b] (μm)
a-Si:He/dynamic	Dynamic	Si	5	150	10	2.96 ± 0.04
a-Si:He/static	Quasistatic	Si	5	150	3	1.16 ± 0.02
a-Si:^{3}He/150 W	Quasistatic	Si/SiC	5	150	14	1.7 ± 0.2
a-Si:^{3}He/200 W	Quasistatic	Si	5	200	20	2.7 ± 0.6[c]
W:He/5 Pa/200 W/static	Quasistatic	Si	5	200	10	1.3 ± 0.1
W:^{3}He/3.5 Pa/200 W	Quasistatic	Si, gold foil	3.5	200	15	0.66 ± 0.01
W:^{3}He/5 Pa/300 W	Quasistatic	Si, gold foil	5	300	16	2.5 ± 0.6[c]

[a] Distance from substrate to target was 10 cm for all samples.
[b] Measured from SEM cross-section (at different positions and cleaved areas).
[c] For these samples and additional profilometry analysis showed Ra roughness also in the range of 0.6 μm.

detectors. The EBS spectra were used to determine the composition of the major elements, while trace elements were derived from the PIXE analysis.

Target stability tests were performed on a W:^{3}He sample with a beam of ^{64}Zn, which was accelerated by the PIAVE-ALPI [35,36] accelerator complex at an energy of 275 MeV and an intensity varying between 0.5 and 5 pnA. For this test experiment, the GALILEO [37] γ-ray array was employed together with the Neutron-Wall [38] neutron detector array and the EUCLIDES [39] light charged particle detector array.

3. Results and discussion

3.1. A quasistatic procedure for magnetron sputtering thin film deposition

The magnetron sputtering procedure is based on the plasma generation, by glow discharge of a low pressure gas, in a chamber equipped with a magnetron head incorporating the target material to be deposited as a cathode. It is usually recommended to establish the working gas pressure in the chamber by introducing a given gas flow and controlling the aperture of a throttle valve that is connected to a continuous pumping system [40]. This dynamic procedure is thought to facilitate the stability of the working pressure and to improve the purity of working gas by a continuous renewal of the gas. A quasistatic procedure has been developed at the Materials Science Institute in Seville (ICMS-CSIC) [27] to carry out the magnetron sputtering deposition procedure under the conditions of a very low consumption of the working gas. In this paper the application of this methodology to the fabrication of ^{3}He-rich solid targets is presented. To the best of our knowledge such a quasistatic procedure was only considered in the context of gas convention studies during Ar sputtering deposition of molibdenum [41] or in a laser-induced chemical vapour deposition of aluminum [42].

Fig. 1 shows a schematic diagram of the deposition chamber and indicates the main components. Special characteristics for the work under low consumption conditions are the needle valve (1) and the small gas tank (50 mL) with a pressure sensor. In contrast to the conditions of dynamic flux, the "to vacuum" throttle valve (2) is closed after the establishment of the residual vacuum conditions. The desired working gas pressure is established by carefully opening and closing the needle valve (1). From this static condition, the plasma can be ignited. Fluctuations in the working gas pressure are then corrected by minimum actions on the needle valve (1) and/or the throttle valve (2), leading to the so-called quasistatic conditions. In addition to the amount of gas (He and ^{3}He in this work) necessary to fill the deposition chamber with very low pressures (3–6 Pa for the gas discharge to occur), the method required only intermittent gas fluxes (several seconds) of a maximum of 0.1 mL/min. Pressure fluctuations are mainly due to gas temperature variations under the plasma discharge and the He/^{3}He gas incorporation into the growing film. Purging of the ^{3}He line and the small gas tank were also conducted by filling and pumping cycles (not under flow conditions). The line and tank are therefore kept under overpressure by refilling when necessary to avoid contamination by air.

To establish the feasibility of the quasistatic methodology, experiments were undertaken to compare amorphous silicon coatings fabricated with helium under dynamic or quasistatic conditions with the same deposition parameters (i.e., working pressure, target to substrate distance and RF source power). The microstructural analysis of the two samples, a-Si:He/dynamic and a-Si:He/static (see Table 1), was

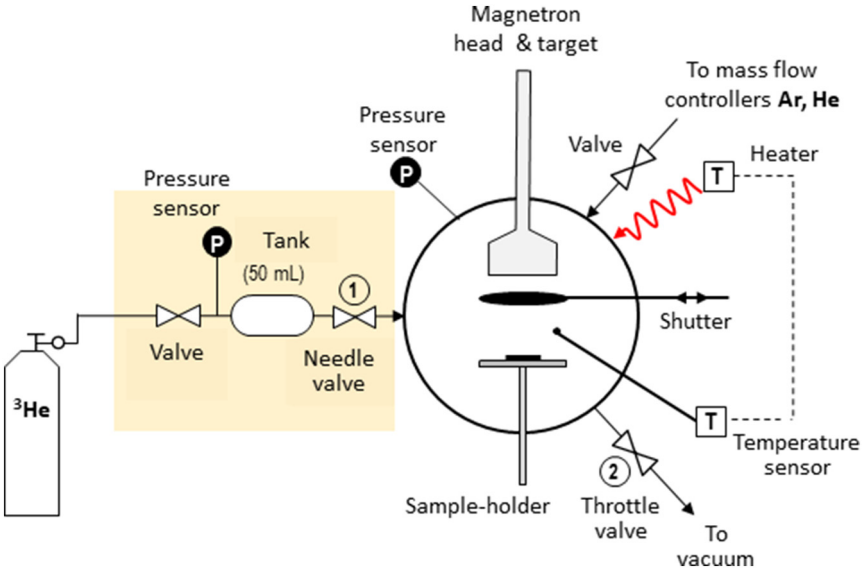

Fig. 1. Scheme of the experimental setup designed for the magnetron sputtering deposition process in static or quasistatic regimes.

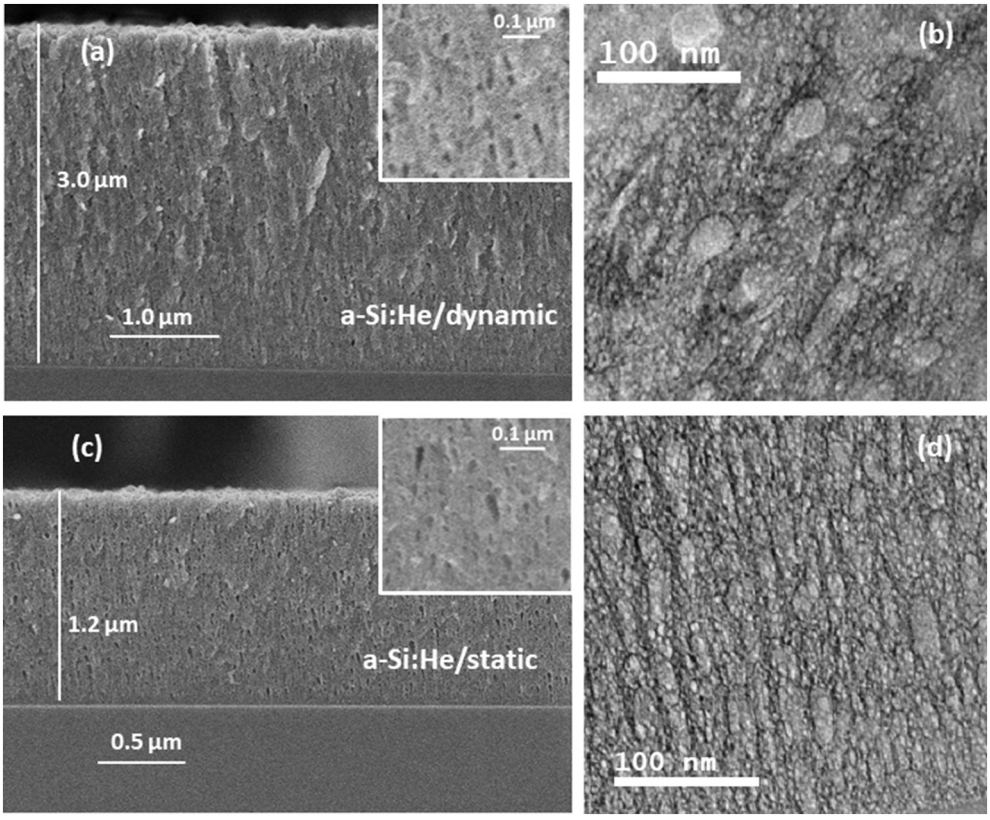

Fig. 2. SEM (a, c) and TEM (b, d) cross section images of the a-Si:He samples grown under dynamic (top) and quasistatic (bottom) conditions.

performed by SEM (see Fig. 2a and c). A similar structure is observed for both samples, with small closed pores already visible (in dark contrast) at low magnification. Tables 1 and 2 summarize film thicknesses (and deposition rates) as evaluated by SEM images. It can be concluded that the work under the quasistatic regime substantially affects neither the formation of nanopores (trapped gas) nor the deposition rate. TEM images at higher magnification in Fig. 2b and d allow the detailed observation of the closed porosity (in bright contrast), showing broad size and aspect ratio distributions of the nanopores (gas bubbles). Pore size and aspect ratio histograms are shown in the supporting information (Fig. S1, ESI) together with a description of the image analysis procedures. Both deposition regimes lead to similar pore size distributions, ranging from a low limit of 0.5 nm to 40 nm. A similar mean size of approximately 7 nm was found for dynamic and quasistatic conditions, with a mean aspect ratio of 0.6 ± 0.2 in both cases. Further details are presented in Fig. S1 and ESI.

A main point is the determination of He content, and possible impurities, in both operational conditions. A summary of the IBA results is included in Table 2 (for atomic % composition) and in Table 3 (for an absolute determination of areal densities given in 10^{18} atom/cm^2). Essentially, Si, He, O, C, N, H, and other possible contaminants from the deposition chamber (i.e., traces of Ti, Cr, Ni, Fe, Cu, and Ta) have been analyzed. Fig. S2 (ESI) presents the p-EBS spectra obtained with a 2.5 MeV proton beam for both samples. The intense peak corresponding to the ^{4}He trapped within the films can easily be observed at approximately 900 keV. The elemental depth profiles derived from IBA for these samples are also shown in Fig. S2. According to these results (see Tables 2 and 3), it can be concluded that neither a significant increase in undesired elements nor a decrease in the ^{4}He content can be observed for the quasistatic regime compared to the dynamic regime for the same experimental conditions. Indeed, considering the uncertainties given in Table 2, the compositions of both samples are indistinguishable from each other, with a ^{4}He incorporation of approximately 29 at.% (that is, ^{4}He/Si ratio of approximately 0.45) and an impurity level <2 at.% for C, O, and N and <7 at.% for H. The only noticeable difference between both films is their thickness, 2.96 ± 0.04 μm for dynamic films and 1.16 ± 0.02 μm for static films, but this difference is simply due to the deposition time used for both films (10 h vs. 3 h, respectively). The helium areal density achieved

Table 2
Deposition rate and composition for the investigated samples.

Sample	Deposition rate[a] (nm·min^{-1})	at.% Si	at.% W	at.% ^{4}He	at.% ^{3}He	at.% C	at.% O	at.% N	at.% H	at.% others[b]
a-Si:He/dynamic	4.9 ± 0.1	64.3 ± 3.8	–	28.1 ± 1.7	–	0.6 ± 0.1	1.6 ± 0.1	<LOD[c]	5.0 ± 0.3	0.5 ± 0.1
a-Si:He/static	6.4 ± 0.2	62.4 ± 1.6	–	28.9 ± 1.3		1.2 ± 0.1	0.8 ± 0.2	<LOD[c]	6.7 ± 0.5	Low < 0.5%
a-Si:^{3}He/150 W	2.0 ± 0.2	78.8 ± 3.0	–	2.0 ± 0.1[d]	15.8 ± 0.6	3.4 ± 0.2	<LOD[c]	Not analyzed	Not analyzed	Low < 0.5%
a-Si:^{3}He/200 W	2.3 ± 0.5	88.8 ± 2.3	–	–	8.4 ± 0.4	1.4 ± 0.1	0.9 ± 0.1	<LOD[c]	0.5 ± 0.1	Low < 0.5%
W:He/5 Pa/200 W/static	2.2 ± 0.2	–	61.5 ± 3.9	24.6 ± 0.7	–	<LOD[c]	4.6 ± 1.0	2.8 ± 0.6	4.4 ± 0.3	2.0 ± 0.4
W:^{3}He/3.5 Pa/200 W	0.73 ± 0.02	–	65.1 ± 3.8	–	7.5 ± 0.8	3.4 ± 0.3	10.6 ± 1.1	<LOD[c]	11.3 ± 0.7	2.0 ± 0.5
W:^{3}He/5 Pa/300 W	2.6 ± 0.6	–	64.6 ± 2.1	–	8.6 ± 0.4	14.4 ± 1.1	2.4 ± 0.3	<LOD[c]	10.1 ± 2.7	Low < 0.5%

[a] Calculated from SEM cross-section images and the deposition time.
[b] Traces of Ti, Cr, Ni, Fe, Cu, Ta.
[c] <LOD: Bellow the limit of detection. Typically 2–3 at.% for N and 1 at.% for C. At the analysis conditions of the a-Si:^{3}He/150 W sample, LOD was 5 at.% for O.
[d] From pipes residual He. The IBA analysis allows unambiguous differentiation of ^{3}He and ^{4}He.

Table 3
Areal densities for the given layer thicknesses of investigated samples.

Sample	Thickness[a] (μm)	Areal density (10^{18} at/cm^2)[b]				At ratio ^{4}He/M[c]	At ratio ^{3}He/M[c]
		^{4}He	^{3}He	Si	W		
a-Si:He/dynamic	2.96 ± 0.04	3.9 ± 0.2	–	8.9 ± 0.5	–	0.44 ± 0.03	–
a-Si:He/static	1.16 ± 0.02	1.70 ± 0.08	–	3.7 ± 0.1	–	0.46 ± 0.02	–
a-Si:^{3}He/150 W	1.7 ± 0.2	0.16 ± 0.01[d]	1.28 ± 0.05	6.4 ± 0.2	–	0.025 ± 0.001	0.20 ± 0.01
a-Si:^{3}He/200 W	2.7 ± 0.6	–	1.12 ± 0.06	11.8 ± 0.3	–	–	0.095 ± 0.005
W:He/5 Pa/200 W/static	1.3 ± 0.1	2.0 ± 0.1	–	–	4.9 ± 0.3	0.41 ± 0.03	–
W:^{3}He/3.5 Pa/200 W	0.66 ± 0.01	–	0.29 ± 0.03	–	2.5 ± 0.1	–	0.12 ± 0.01
W:^{3}He/5 Pa/300 W	2.5 ± 0.6	–	1.10 ± 0.05	–	8.3 ± 0.3	–	0.13 ± 0.01

[a] Calculated from SEM cross-section images.
[b] Determined by p-EBS for the total thickness.
[c] M refers to Si or W.
[d] From pipes residual He. The IBA analysis allows unambiguous differentiation of ^{3}He and ^{4}He.

for the a-Si:He/static sample is 1.7×10^{18} at/cm^2 for 1.16 μm thickness. These are very important results in this work, as the quasistatic methodology is validated as an adequate low gas consumption option for the fabrication of these targets. The capability of reproducing the results when changing from dynamic to static conditions, while keeping the deposition parameters (sputtering power, working gas pressure and target to sample-holder distance), is a good indication of the reproducibility of the sputtering methodology.

An important final consideration in this section is the evaluation of the gas consumption reduction of the quasistatic vs dynamic regime. For the fabrication of the a-Si:He/dynamic sample a continuous helium flow of 50 mL/min was used. For comparison in the quasistatic experiment only punctual fluxes of maximum 0.1 mL/min (according to specifications of the needle valve) were used for a few seconds. Therefore the gas consumption reduction has been estimated to be in any case higher than 99.5%, even considering preliminary steps for He plasma stabilization in the quasistatic regime.

3.2. Fabrication under quasistatic conditions and characterization (microstructural and chemical) of a-Si:^{3}He, W:He and W:^{3}He layers

Fabrication of Si- and W-based films has been undertaken in a ^{3}He plasma under quasistatic conditions that guarantee the very low consumption of the process gas. For comparative purposes, a W:He sample has also been prepared in the quasistatic regime. Although previous papers have reported ^{3}He solid targets fabricated by ion implantation [43,44] or under cryogenic conditions [45], the gas consumption was to our knowledge not optimized in previous works. In this section of the paper, in addition to the extremely low ^{3}He consumption, the performance of the fabricated targets is reported with respect to the trapped gas amount, target homogeneity (vertical distribution of trapped gas), and control of impurities. An additional advantage of the presented procedure is the use of MS, a well-established and relatively inexpensive technology, widely used on an industrial scale for the production of layers and coatings.

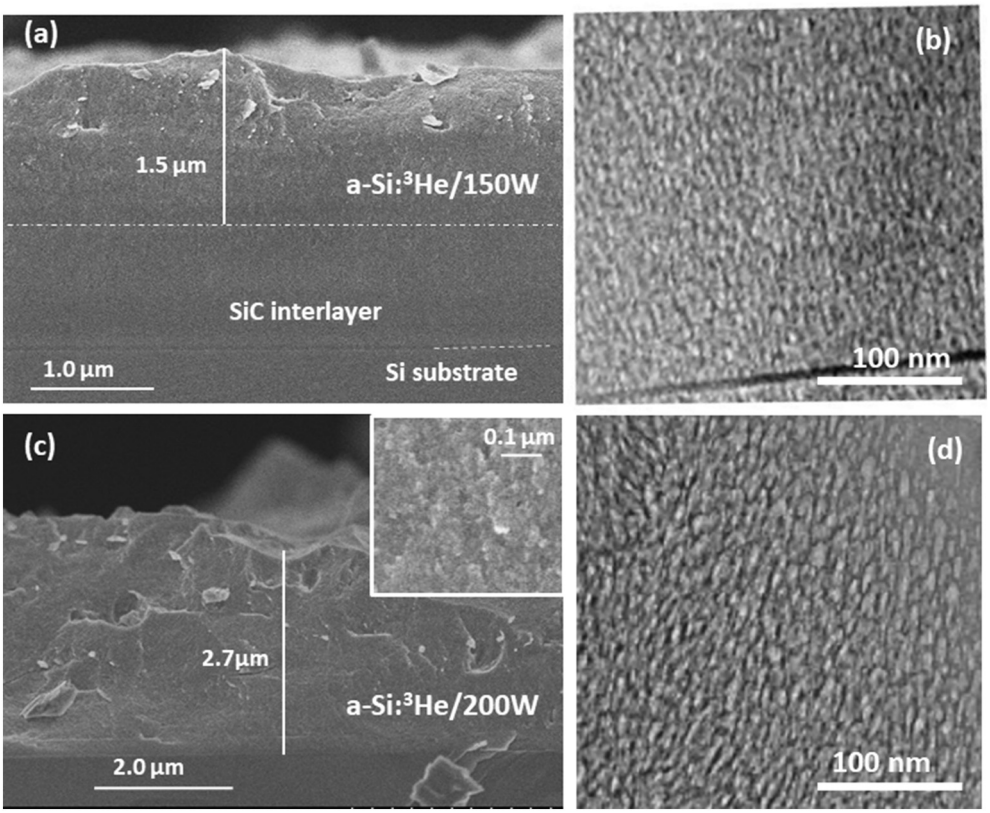

Fig. 3. SEM (a, c) and TEM (b, d) cross section images of the a-Si:^{3}He/150 W (top) and a-Si:^{3}He/200 W (bottom) samples.

3.2.1. The a-Si:^{3}He layers

First, two amorphous Si:^{3}He samples were grown with RF power of 150 and 200 W (see Table 1). Fig. 3 presents the SEM and TEM images for both samples. Cross sectional SEM (a and c) allows one to determine the thicknesses of the deposited layers. The SiC interlayer shown for the a-Si:^{3}He/150 W sample has been highlighted by IBA (see Fig. 4 and details below). Variations in thicknesses are observed in these samples due to surface roughness, especially for the a-Si:^{3}He/200 W sample. Some closed pores are visible as dark contrast features by SEM in the high magnification inset in Fig. 3c. Nevertheless, only the high resolution TEM images (b and d) could unambiguously demonstrate the presence of the closed nanoporosity (bright contrast features with trapped gas). In a general observation, smaller and narrower pore size distributions were found for the samples grown with ^{3}He (~4 nm; see Fig. S3), compared to the natural He samples (~7 nm; see Fig. S1). Additionally, larger pores are not observed for Si:^{3}He films, while smaller and elongated pores were profusely present, as indicated by their aspect ratio histograms (see Fig. S3), which showed a mean value approximately 0.5 (vs. ~0.6 for Si:^{4}He films; see Fig. S1).

Once again, atomic compositions and areal densities derived from IBA analysis are summarized in Tables 2 and 3. Fig. 4 (left) shows the p-EBS spectra obtained with a 2.5 MeV proton beam for both a-Si:^{3}He samples, where the intense peak arising at approximately 650 keV corresponds to the ^{3}He trapped within the Si-based films. For a-Si:^{3}He/150 W, a small ^{4}He signal, likely arising from residual pipe He, was also detected (signal approximately at 900 keV). This result shows the unambiguous differentiation of ^{3}He and ^{4}He by IBA. Depth profiles derived from IBA are presented for both samples in Fig. 4 (right). For a-Si:^{3}He/150 W, the formation of a SiC interlayer (grown during the first steps of deposition) and the top growth of the Si:^{3}He layer are demonstrated. For the thickest a-Si:^{3}He/200 W sample, the profiles (stepped shape) are also in agreement with the larger thickness variation (roughness) observed by SEM for this sample. The obtained results in Tables 2 and 3 allow us to conclude that ^{3}He is incorporated in both samples, with a maximum of 16 at.% achieved for the layer grown at 150 W. Regarding the impurities (i.e., C, O, N and H), their level remains below 4 at.% for both samples. The helium areal density achieved for the sample grown at 150 W is $(1.3 \pm 0.1) \times 10^{18}$ at/cm^2 for (1.7 ± 0.2) μm film thickness and a ^{3}He/Si atomic ratio of 0.20 ± 0.01.

These results present, for the first time, the fabrication of ^{3}He solid targets based on the magnetron sputtering deposition methodology under quasistatic low gas consumption conditions. The higher ^{3}He/Si atomic ratio incorporated at 150 W, as compared to 200 W, can be explained for similar pores densities as a consequence of the higher average pore size at higher voltage (~3 nm for 150 W *vs* ~5.5 nm for 200 W, see Fig. S3). According to previous results with Si:He samples grown under dynamic regimen, higher voltages lead to bigger pores which stabilize lower He densities [18–20].

The obtained results in this section also show that moving from ^{4}He to ^{3}He (for the same experimental conditions) leads to a significant reduction in the process gas incorporation from ^{4}He/Si ≈ 0.45 to ^{3}He/Si ≈ 0.20. In Section 3.1, we have demonstrated that there is not influence in

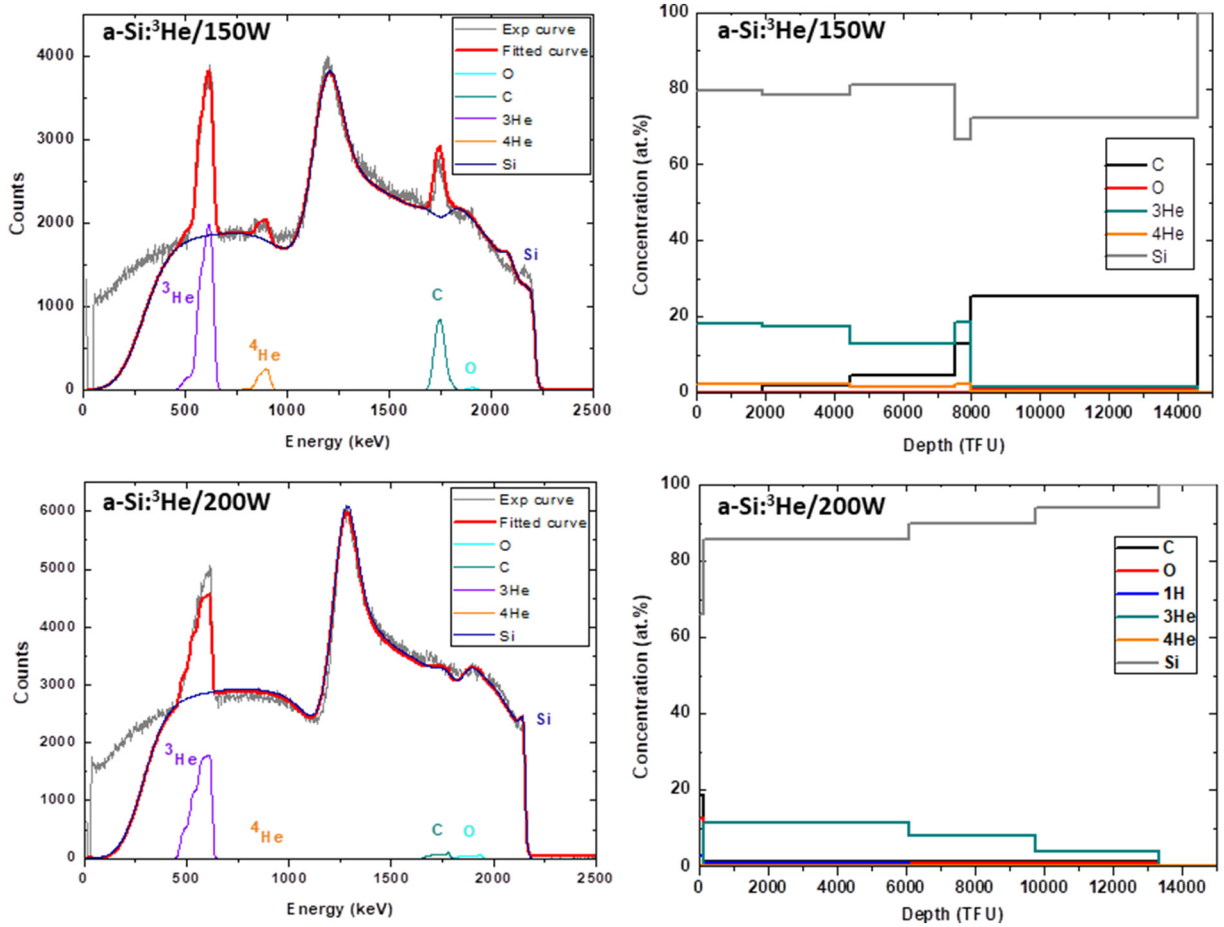

Fig. 4. Left: Experimental proton EBS-spectra (dark grey curves) acquired at 165 degrees and 2.5 MeV from the a-Si:^{3}He/150 W and a-Si:^{3}He/200 W samples, along with the fitted curves (red) and the separate contributions of elemental curves (O in cyan, C in dark green, ^{3}He in purple, ^{4}He in orange, and Si in dark blue). Right: Elemental depth profiles derived from Total-IBA analysis (i.e., combining various beam conditions as described in the experimental section). The depth profile for the a-Si:^{3}He/150 W shows the presence of a SiC interlayer, while the Si gradient observed in the a-Si:^{3}He/200 W can be attributed to the roughness of coating. (For interpretation of the references to colour in this figure legend, the reader is referred to the web version of this article.)

the He content when moving from dynamic to quasistatic regime, therefore the difference may be due to an intrinsic behaviour of the film growth under ^{4}He compared to ^{3}He plasma.

3.2.2. The W:He and W:^{3}He layers

Tungsten was selected with the aim of investigating a high atomic number matrix material. W is metallic, leads to polycrystalline films by sputtering and was tested in this work by quasistatic magnetron sputtering deposition with both ^{3}He and natural He plasmas. Samples were grown with RF power of 200 W and 300 W (Table 1).

Fig. 5a and b respectively present the SEM and TEM images for the W:He/5 Pa/200 W/static sample grown with natural He. The cross sectional SEM image was used for thickness determination and shows a more granular texture for the polycrystalline W in comparison to amorphous silicon. Dark contrast features in the SEM images (see Fig. S4) already indicate the presence of closed pores (with trapped gas) that are much better observed as bright contrast features in the high resolution TEM image (Fig. 5b). Closed pores have broad size and shape distributions (see Fig. S5). The mean pore size of ^{4}He bubbles trapped in a W matrix was found to be smaller (~5 nm) than that of the ^{4}He bubbles trapped in Si-based films grown under similar conditions (~7 nm; Fig. S1). Regarding the mean aspect ratio, W-based films are found to be similar to Si-based films, with a mean value of 0.6 indicating the formation of elongated pores. Elemental composition derived from IBA gives values of 25 at.% for ^{4}He incorporation, with impurity levels below 5 at.% for C, O, N and H (See Tables 2 and 3). Helium areal densities for this sample achieved $(2.0 \pm 0.1) \times 10^{18}$ at/cm^2 for (1.3 ± 0.1) μm thickness and a He/W atomic ratio of 0.41 ± 0.03. It is worth mentioning that the amount of trapped helium in the case of tungsten is smaller than the one obtained with ^{4}He in a Si matrix at 150 W (a-Si:He/static sample). This effect is mostly due to the lower pore density obtained in the case of tungsten as observed in the TEM images (Fig. 5b vs Fig. 2d). Fig. 5c shows the p-EBS spectra obtained from this sample, with the intense ^{4}He peak arising at approximately 900 keV. These are important results in this work because the quasistatic methodology is also validated for the W:He system.

Fig. 6a and b present the SEM cross sectional images obtained for the W:^{3}He/3.5 Pa/200 W and W:^{3}He/5 Pa/300 W samples grown with ^{3}He. In addition to thickness determination (Table 1), the images also show a more granular texture, which is characteristic for the polycrystalline W (this was already observed for the natural He case). Closed pores are clearly visible as bright contrast features in a representative high resolution TEM image for the W:^{3}He/3.5 Pa/200 W sample (Fig. 6c). The pore size and shape distribution histograms are shown in Fig. S5 (ESI). A mean pore size of approximately 2 nm was found for the W:^{3}He/3.5 Pa/200 W sample, which is significantly smaller than the mean pore size of W:^{4}He (~5 nm). As in the case of silicon, the change from natural He to ^{3}He leads to narrower distributions and smaller sizes of the trapped bubbles. Regarding the mean aspect ratio, the values are in agreement with elongated pores with an average aspect ratio of 0.6. The elemental composition derived from IBA gives ^{3}He contents of approximately 8 at.%. Fig. 6d illustrates the representative p-EBS spectra obtained for the W:^{3}He/5 Pa/300 W sample, with the ^{3}He peak arising at approximately 650 keV. The helium areal density obtained for this sample (the thicker one) is $(1.10 \pm 0.05) \times 10^{18}$ at/cm^2 for (2.5 ± 0.6) μm thickness and a He/Si atomic ratio of 0.13 ± 0.01. It is worth mentioning that, similarly to Si-based films, the ^{3}He incorporation in W is lower compared to ^{4}He. This is remarkable in the case of the W:^{3}He samples due to a lower pore density. The main drawback for both W:^{3}He samples is the impurity levels for C, O, and H, which can reach values of over 10 at.%. These contaminants, as present in the residual chamber vacuum, appear to be more reactive for W than for Si in the activated plasma phase. The effect is more remarkable for ^{3}He than for ^{4}He. Careful work by following ultra-high-vacuum procedures (e.g.

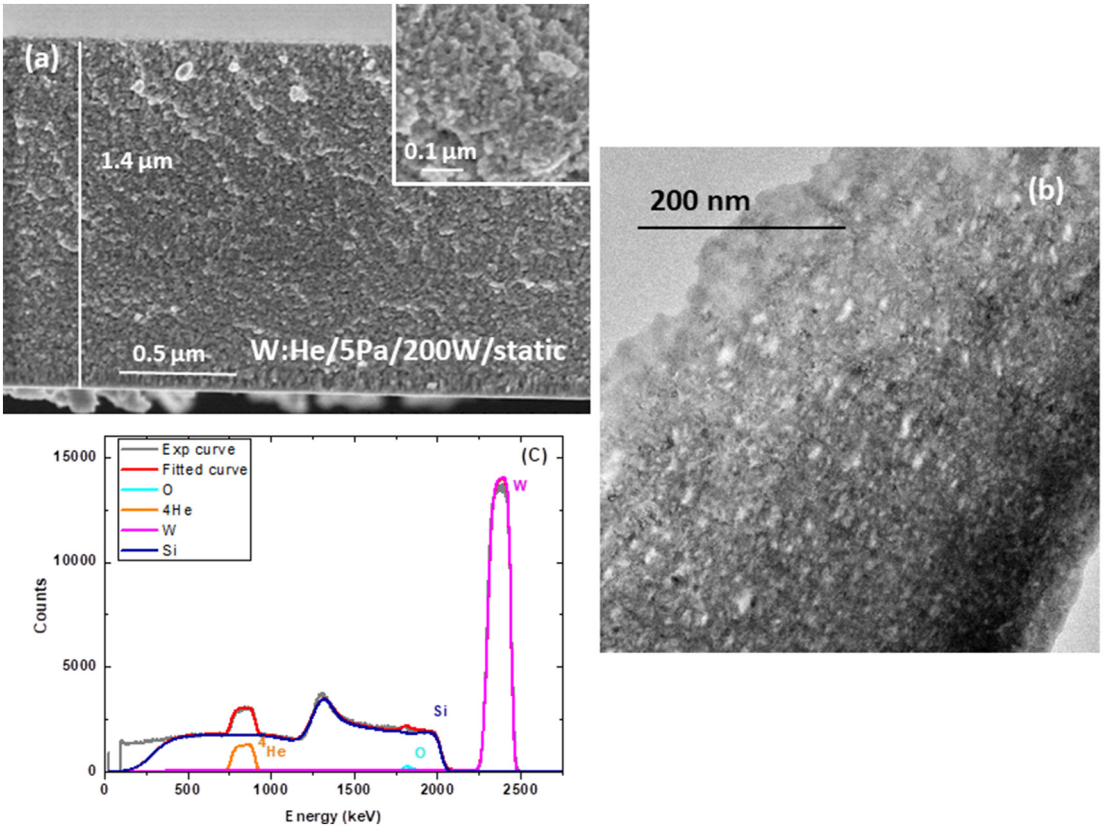

Fig. 5. (a) SEM images of the W:He/5 Pa/200 W/static sample grown on a Si substrate. (b) TEM image of this sample with pores visible as bright contrast areas. (c) Experimental proton EBS-spectrum (dark grey) acquired at 165 degrees and 2.5 MeV along with the fitted curve (red) and the separate elemental curves (O in cyan, ^{4}He in orange, W in magenta, and Si in dark blue). (For interpretation of the references to colour in this figure legend, the reader is referred to the web version of this article.)

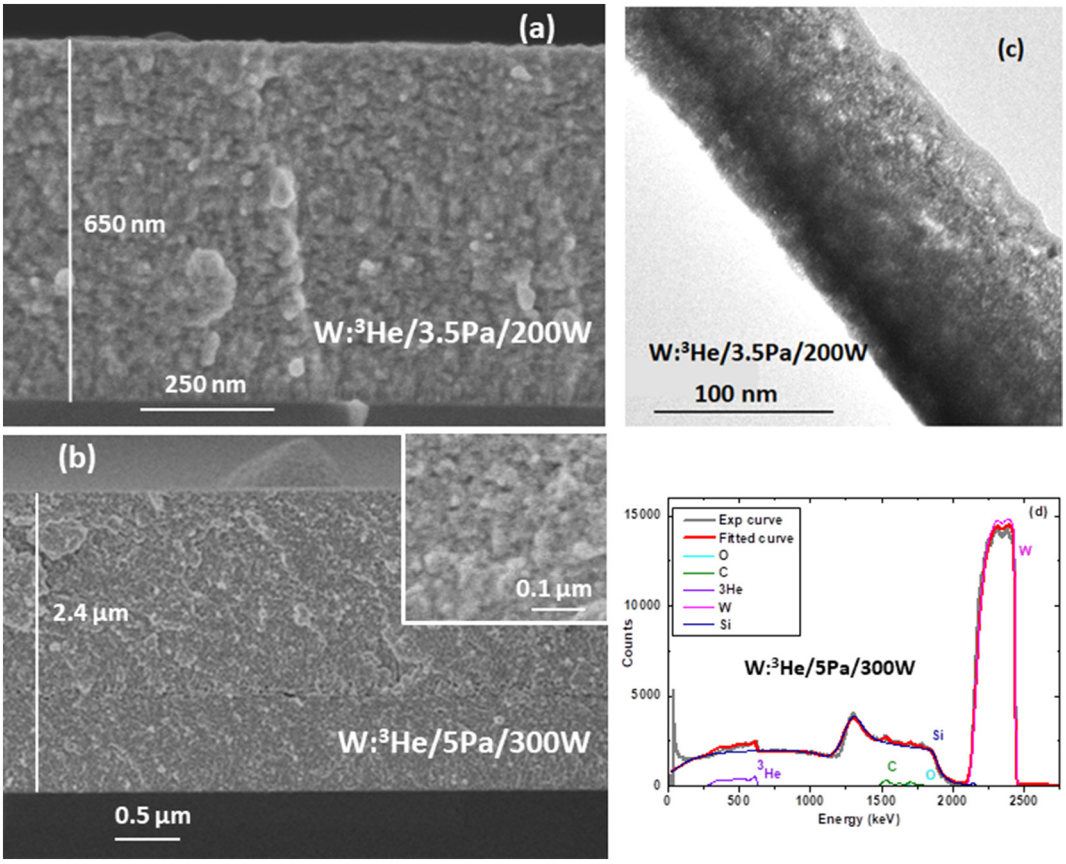

Fig. 6. (a, b) SEM images of the W:^{3}He/3.5 Pa/200 W and W:^{3}He/5 Pa/300 W samples grown on a Si substrate. (c) Representative TEM image of the W:^{3}He/3.5 Pa/200 W sample with pores visible as bright contrast areas. (d) Experimental proton EBS-spectra (dark grey) acquired at 165 degrees and 2.5 MeV from the W:^{3}He/5 Pa/300 W sample along with the fitted curve (red) and the separate elemental curves (O in cyan, C in dark green, 3He in purple, W in magenta and Si in dark blue). (For interpretation of the references to colour in this figure legend, the reader is referred to the web version of this article.)

baking installations, exclusive use of copper gaskets) in conjunction with better target purity and cleaning will address this concern. Nevertheless we have been able to demonstrate the incorporation of ^{3}He in tungsten by the proposed bottom-up methodology. The advantage of low gas consumption and the possibility to increase, by increasing the film thicknesses, the total amount of ^{3}He up to the range of 10^{18} at/cm^2 areal densities are clearly demonstrated in this work. In addition further work is still needed to screen the process parameters seeking for optimization of the ^{3}He incorporation.

3.3. First experiments to probe stability of the targets for nuclear reaction studies

One of the main concerns with the new targets was the possible evaporation of ^{3}He during experiments, mainly due to heating caused by the probe beam energy loss. In particular, the stability of the supported W:^{3}He/3.5 Pa/200 W film, as solid target for experiments in inverse kinematics, was investigated in this work. The EUCLIDES array was used according to descriptions in the experimental section. The ^{3}He was expelled out of the target due to the elastic scattering with the ^{64}Zn probe beam and was detected in the ΔE-E telescopes. The counting rate is directly proportional to the density of ^{3}He inside the target; therefore, by monitoring this value, it was possible to determine the effect of evaporation. The result is presented in Fig. 7, which shows the change in the counting rate normalized over the beam intensity as a function of time. In the span of 11 h, even with beam current between 2.4 and 5 pnA, the rate decreases by a factor of 3.

While ^{3}He does indeed evaporate from the target, as expected, the stability is deemed excellent. It may be considered that envisaged experiments in inverse kinematic configuration will utilize this kind of target

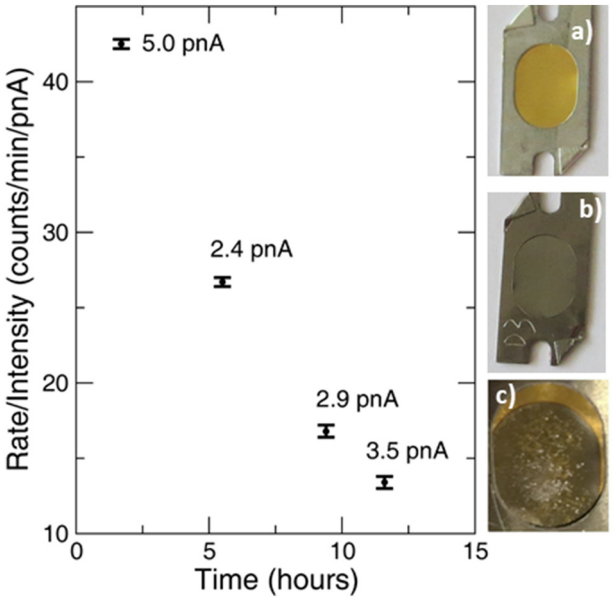

Fig. 7. (Left) Counting rate for one of the forward EUCLIDES detectors of the ^{3}He signal for the W:^{3}He/3.5 Pa/200 W sample as a function of the beam irradiation time with a ^{64}Zn probe beam at 275 MeV energy. The rate is normalized over the beam intensity. (Right) Photographs of the gold foil support in a frame before deposition (a) and the deposited W film with ^{3}He as prepared (b) and after the inverse kinematic experiment (c). (For interpretation of the references to colour in this figure legend, the reader is referred to the web version of this article.)

with RIBs (radioactive ion beams), the intensity of which is expected to be 4–5 orders of magnitude lower than that of the beam used in this experiment. In those conditions, the impact of ^{3}He evaporation from target may be negligible. The stabilization of the trapped nanobubbles within the solid matrix additionally leads to an easy handling and a high stability for years [17] of these targets under ambient conditions. It has been also included in Fig. 7 macroscopic photographic visualizations of the gold foil support in a frame before deposition (a); as well as, the deposited W film with ^{3}He both as prepared (b) and after the experiment in inverse kinematic harsh conditions (c). Further work is still needed to understand film growth mechanism and the role of process parameters in bubbles formation and total amount of trapped helium. Improvement of gas content would facilitate future experiments.

4. Conclusions

A methodology based on the magnetron sputtering technique has been proposed to be operated in quasistatic flux conditions to produce nanoporous films to stabilize gas nanobubbles. Films composed of the sputtered material with entrapped plasma process gas have therefore been produced for application as targets for nuclear reactions involving this trapped gas. The static mode of operation has been shown to be much more advantageous due to the low gas consumption of scarce gases such as ^{3}He. The gas used for filling the deposition chamber at low pressures (3–6 Pa) and punctual fluxes (several seconds) at the maximum flow rate of 0.1 mL/min represented the only consumption under operation. Gas consumption reduction of >99.5% was achieved as compared to conventional sputtering under dynamic conditions. Our experiments show no significant changes regarding helium content or purity when comparing dynamic and static deposition for the same matrix elements (Si and W in this work), the same He isotope (^{3}He and ^{4}He) and the same deposition parameters. Deposition on different substrates was demonstrated. Analytical data also show that transitioning from ^{4}He to ^{3}He, for the same experimental conditions, leads to a reduction of helium incorporation for both Si and W matrices. This effect is not a question of the static mode but rather a question of intrinsic behaviour of the ^{4}He compared to ^{3}He plasma. It is also clear that Si-based samples are rather clean in terms of the incorporation of impurities. However, major contaminants, such as carbon, oxygen and hydrogen (as present in the chamber's residual vacuum), appear to be much more reactive to the W film growth. Ultra-high vacuum procedures in conjunction with better target purity improve this point. The ^{3}He content achieved was over 1×10^{18} at/cm^{2} for film thicknesses between 1.5 and 3 μm for both Si and W matrices. This result means that it has been possible to achieve targets with ^{3}He contents ≥6 μg/cm^{2}. Although the results with ^{3}He presented in this work can still be improved (from ^{3}He content and target purity points of view), the presented methodology is opening promising new directions for the fabrication of solid targets of scarce isotopes, such as ^{3}He, ^{21}Ne and others. The first validation tests of the targets have shown adequate stability for nuclear reaction studies under the conditions of inverse kinematic experiments.

The simplicity, low cost and versatility of the presented methodology opens new pathways to develop these targets. Investigations with alternative gases and isotopes, on-demand selection of matrix elements, target presentation (self-supported, multilayers), or introduction of flexible substrates are now possibilities for further works. On-demand design of the targets can be therefore done in a case by case basis.

CRediT authorship contribution statement

Asunción Fernández: Conceptualization, Methodology, Formal analysis, Funding acquisition, Writing - original draft.**Dirk Hufschmidt:** Methodology, Data curation, Formal analysis, Writing - review & editing.**Julien L. Colaux:**Data curation, Formal analysis, Writing - review & editing.**Jose J. Valiente-Dobón:**Data curation, Formal analysis, Funding acquisition, Writing - review & editing.**Vanda Godinho:**Data curation, Formal analysis, Writing - review & editing.**Maria C. Jiménez de Haro:**Data curation, Formal analysis, Writing - review & editing. **David Feria:**Data curation, Formal analysis.**Andrés Gadea:**Formal analysis, Funding acquisition, Writing - review & editing.**Stéphane Lucas:**Formal analysis, Funding acquisition, Writing - review & editing.

Declaration of competing interest

The authors declare that they have no known competing financial interests or personal relationships that could have appeared to influence the work reported in this paper.

Acknowledgements

This work was supported by the Spanish Ministry of Science, Innovation and Universities and co-financed by EU FEDER funds under the following grants: RTI2018-093871-B-I00, CTQ2015-65918-R, FPA2017-84756-C4 and SEV-2014-0398. CSIC support under grant PIE-201760E002 is also acknowledged. A.F. thanks the Spanish Ministry for granting her with a visiting researcher fellowship at the Univ. Namur. Authors thank the Laboratory for Nanoscopies and Spectroscopies (LANE) for the TEM facilities and the technical assistance of J. López, O. Montes, I. Rosa, and M.R. García.

Appendix A. Supplementary data

Pores distribution analysis from TEM images (pore size and aspect ratio histograms), IBA characterization of the a-Si:^{4}He samples, enlarged SEM image for pores visualization. Supplementary data to this article can be found online at https://doi.org/10.1016/j.matdes.2019.108337.

References

[1] S.D. Pain, Advances in instrumentation for nuclear astrophysics, AIP Adv. 4 (2014), 041015(14 pp.).
[2] A. Obertelli, T. Uesaka, Hydrogen targets for exotic-nuclei studies developed over the past 10 years, Eur. Phys. J. A 47 (2011) 105.
[3] K.E. Rehm, J.P. Greene, B. Harss, D. Henderson, C.L. Jiang, R.C. Pardo, B. Zabransky, M. Paul, Gas cell targets for experiments with radioactive beams, Nucl. Instrum. Methods Phys. Res. A 647 (2011) 3–9.
[4] L.C. Jarrott, M.S. Wei, C. McGuffey, et al., Visualizing fast electron energy transport into laser-compressed high-density fast-ignition targets, Nat. Phys. 12 (2016) 499–504.
[5] A. Curtis, C. Calvi, J. Tinsley, et al., Micro-scale fusion in dense relativistic nanowire array plasmas, Nat. Commun. 9 (2018) 1077(7 pp.).
[6] A. Stolarz, Target preparation for research with charged projectiles, J. Radioanal. Nucl. Chem. 299 (2014) 913–931.
[7] J. Walshe, M. Freer, C. Weldhon, et al., The thick target inverse kinematics technique with a large acceptance silicon detector array, J. Phys. Conf. Ser. 569 (2014), 012052 (4 pp.).
[8] Cyclotron produced radionuclides: principles and practice, IAEA Technical Report Series No. 465, IAEA, Vienna, 2008 , ISBN 978–92–0–100208–2.
[9] G.F. Knoll, Radiation Detection and Measurement, 4th edition Wiley, 2010.
[10] F. Vanderbist, C. Angulo, M. Couder, Y. El Masri, P. Leleux, M. Loiselet, G. Tabacaru, Realization and analysis of He-implanted foils for the measurement of (α, γ) reaction cross-sections in nuclear astrophysics, Nucl. Instrum. Methods Phys. Res. B 197 (2002) 165–171.
[11] L. Weissman, R. Raabe, M. Huyse, G. Koops, H. Pattyn, G. Terwagne, P. Van Duppen, An implanted ^{4}He target for experiments with radioactive beams, Nucl. Instrum. Methods Phys. Res. B 170 (2000) 266–275.
[12] K. Schmidt, K.A. Chipps, S. Ahn, D.W. Bardayan, J. Browne, U. Greife, Z. Meise, F. Montes, P.D. O'Malley, W.-J. Ong, S.D. Pain, H. Schatz, K. Smith, M.S. Smith, P.J. Thompson, Status of the JENSA gas-jet target for experiments with rare isotope beams, Nucl. Instrum. Methods Phys. Res. A 911 (2018) 1–9.
[13] T. Griegel, H.W. Drotleff, J.W. Hammer, H. Knee, K. Petkau, Physical properties of a heavy-ion-beam-excited supersonic jet gas target, J. Appl. Phys. 69 (1) (1991) 19–22.
[14] P. Dolégiéviez, A. Gillibert, W. Mittig, et al., A cryogenic target for direct reaction studies with exotic beams, Nucl. Instrum. Methods Phys. Res. A 564 (2006) 32–37.
[15] Y. Ayyad, D. Bazin, S. Beceiro-Novo, M. Cortesi, W. Mitting, Physics and technology of time projection chambers as active targets, Eur. Phys. J. A 54 (2018) 181(45 pp.).
[16] S. Beceiro-Novo, T. Ahn, D. Bazin, W. Mittig, Active targets for the study of nuclei far from stability, Prog. Part. Nucl. Phys. 84 (2015) 124–165.
[17] V. Godinho, F.J. Ferrer, B. Fernández, J. Caballero-Hernández, J. Gómez Camacho, A. Fernández, Characterization and validation of a-Si magnetron-sputtered thin films

as solid he targets with high stability for nuclear reactions, ACS Omega 1 (2016) 1229–1238.
[18] V. Godinho, J. Caballero-Hernández, D. Jamon, T.C. Rojas, R. Schierholz, J. García-López, F.J. Ferrer, A. Fernández, A new bottom-up methodology to produce silicon layers with a closed porosity nanostructure and reduced refractive index, Nanotechnology 24 (2013), 275604(10 pp.).
[19] R. Schierholz, B. Lacroix, V. Godinho, J. Caballero-Hernández, M. Duchamp, A. Fernández, STEM–EELS analysis reveals stable high-density He in nanopores of amorphous silicon coatings deposited by magnetron sputtering, Nanotechnology 26 (2015), 075703(10 pp.).
[20] B. Lacroix, V. Godinho, A. Fernández, The nanostructure of porous cobalt coatings deposited by magnetron sputtering in helium atmosphere, Micron 108 (2018) 49–54.
[21] A. Dewald, O. Möller, P. Petkov, Developing the Recoil Distance Doppler-Shift technique towards a versatile tool for lifetime measurements of excited nuclear states, Prog. Part. Nucl. Phys. 67 (2012) 786–839.
[22] H. Zheng, S. Liu, B. Yu, L.B. Wang, C.Z. Liu, L.Q. Shi, Introduction of helium into metals by magnetron sputtering deposition method, Mater. Lett. 59 (2005) 1071–1075.
[23] Z. Han, C. Wang, L. Shi, Synthesis and characterization of helium-charged titaniumhydride films deposited by direct current magnetron sputtering with mixed gas, Mater. Des. 119 (2017) 180–187.
[24] L.J. Atherton, Targets for the national ignition campaign, J. Phys. Conf. Ser. 112 (2008), 032063.
[25] J. Schreiber, P.R. Bolton, K. Parodi, "Hands-on" laser-driven ion acceleration: a primer for laser-driven source development and potential applications, Rev. Sci. Instrum. 87 (2016), 071101.
[26] L.J. Wittenberg, E.N. Cameron, G.L. Kulcinski, S.H. Ott, J.F. Santarius, G.I. Sviatoslavsky, I.N. Sviatoslavsky, H.E. Thompson, A review of ^{3}He resources and acquisition for use as fusion fuel, Fusion Technology 21 (1992) 2230–2253.
[27] A. Fernández, D. Hufschmidt, V. Godinho, M.C. Jiménez de Haro, Spanish patent application No. P201831107, Procedimiento de obtención de un material sólido con agregados gaseosos mediante pulverización catódica por magnetrón en condiciones estáticas o cuasiestáticas para reducir el consumo de gas, patent filed on 15 Nov 2018.
[28] W.S. Rasband, ImageJ, U. S. National Institutes of Health, Bethesda, Maryland, USA, 1997–2018. https://imagej.nih.gov/ij/.
[29] C. Jeynes, J.L. Colaux, Thin film depth profiling by ion beam analysis, Analyst 141 (21) (2016) 5944–5985.
[30] J.L. Colaux, G. Terwagne, C. Jeynes, On the traceably accurate voltage calibration of electrostatic accelerators, Nucl. Instrum. Methods Phys. Res. B 349 (2015) 173–183.
[31] A.F. Gurbich, I. Bogdanović Radović, Z. Siketić, M. Jaksić, Measurements and evaluation of the cross-section for helium elastic scattering from nitrogen, Nucl. Instrum. Methods Phys. Res. B 269 (2011) 40–44.
[32] E.V. Gai, A.F. Gurbich, Evaluated ^{12}C(^{4}He,^{4}He)^{12}C cross-section and its uncertainty, Nucl. Instrum. Methods Phys. Res. B 296 (2013) 87–91.
[33] R.A. Langley, Techniques for studying hydrogen and helium isotopes in materials: ion backscattering and nuclear microanalysis, Proc. Int. Conf. on Radiation Effect and Tritium Technology for Fusion Reactors IV 1976, p. 158.
[34] A.F. Gurbich, SigmaCalc recent development and present status of the evaluated cross-sections for IBA, Nucl. Instrum. Methods Phys. Res. B 371 (2016) 27–32.
[35] A. Lombardi, G. Bisoffi, A. Pisent, et al., Status of PIAVE, LNL-INFN Annual Report, 2003 199.
[36] G. Fortuna, R. Pengo, G. Bassato, et al., The ALPI project at the laboratory Nazionali di Legnaro, Nucl. Instrum. Methods Phys. Res. A 287 (1990) 253–256.
[37] J.J. Valiente-Dobón, D. Mengoni, F. Recchia, et al., Status of the gamma-ray spectrometer GALILEO, LNL-INFN Annual Report 2014, p. 95.
[38] Ö. Skeppstedt, H.A. Roth, L. Lindström, et al., The EUROBALL neutron wall — design and performance tests of neutron detectors, Nucl. Instrum. Methods Phys. Res. A 421 (1999) 531–541.
[39] D. Testov, D. Mengoni, C. Boiano, et al., The first physical campaign of the EUCLIDES Si-ball detector coupled to GALILEO gamma-ray spectrometer, LNL-INFN Annual Report 2015, p. 105.
[40] R.V. Stuart, Vacuum Technology, Thin Films and Sputtering: An Introduction, Academic Press Inc, New York, 1983.
[41] D.W. Hoffman, A sputtering wind, J. Vac. Sci. Technol. A 3 (3) (1985) 561–566.
[42] T.H. Baum, C.E. Larson, R.L. Jackson, Laser-induced chemical vapor deposition of aluminum, Appl. Phys. Lett. 55 (12) (1989) 1264–1266.
[43] A.A. Naqvi, A. Aksoy, M.M. Nagadi, M.A. Al-Ohali, S. Kidwai, O. Fageeha, Fabrication and tests of ^{3}He and ^{2}H targets for beam polarization measurement, Appl. Radiat. Isot. 53 (2000) 439–442.
[44] W.H. Geist, Z. Ayer, A.C. Hird, E.J. Ludwig, M. Wood, K.A. Fletcher, Ion implanted ^{3}He targets for very low energy experiments, Nucl. Instrum. Methods Phys. Res. B 111 (1996) 176–180.
[45] C.D. Keith, C.R. Gould, D.G. Haase, P.R. Huffman, N.R. Roberson, M.L. Seely, W. Tornow, W.S. Wilburn, A polarized solid ^{3}He target for neutron transmission experiments, Nucl. Instrum. Methods Phys. Res. A 357 (1995) 34–39.